

Enhanced cooperativity of J-exciton-polaritons in dielectric BIC metasurfaces

Marco Marangi,^{1,2} Alexander M. Dubrovkin,^{1,2} Anton N. Vetlugin,^{1,2} Giorgio Adamo,^{1,2*} Cesare Soci^{1,2*}

¹ Centre for Disruptive Photonic Technologies, The Photonics Institute, Nanyang Technological University, Singapore 637371

² Division of Physics and Applied Physics, School of Physical and Mathematical Sciences, Nanyang Technological University, Singapore 637371

*Correspondence to: g.adamo@ntu.edu.sg; csoci@ntu.edu.sg

Sources of highly correlated photons are critical for non-linear optics, emerging quantum information, communication and sensing technologies, as well as for fundamental studies of light-matter interaction. A strategy to realize such sources relies on the cooperative coupling of quantum emitters, enabling collective light emission known as superradiance. Here, we demonstrate that organic molecular J-aggregates exhibit room temperature superradiant emission that transitions to a highly collective regime of ~ 250 synchronized J-excitons when strongly coupled to delocalized photonic modes of a silicon bound-state-in-the-continuum metasurface. This enhanced cooperativity manifests as a Rabi splitting dependent scaling of both emission rate and intensity, driving the system into a superbunching regime of photon statistics. At the highest excitation density, we observe *massively superbunched* photon emission with $g_{(\tau=0)}^{(2)} > 13$, unlocking new possibilities for engineering ultrafast, temporally correlated light sources that can operate at room temperature.

Keywords: Bound-states-in-the-continuum (BIC) metasurfaces; exciton-polaritons; J-aggregates; temporal photon correlations; cooperative emission; superradiance; superbunching.

Main

Cooperative phenomena such as superradiance (SR) and superfluorescence (SF) have long captivated researchers for their rich many-body physics. Nowadays, there is resurgent interest in cooperative effects in solid state emitters^{1,2} as a platform to generate strongly correlated photons³⁻⁷ that find application in high quality ghost imaging^{8,9} and multi-photon microscopy¹⁰⁻¹⁵, enhanced non-linear optical processes¹⁶⁻¹⁸, high-performance light detection and ranging¹⁹, and secure quantum key distribution (QKD) protocols²⁰⁻²³.

First introduced by Dicke in 1954, superradiance describes the spontaneous synchronization of N emitters through their interaction with a common radiation field within a λ^3 volume²⁴. This collective behaviour gives rise to a macroscopic dipole moment that results in ultrafast bursts of coherent photons of super-Poissonian distribution, radiative decay rate scaling with N , and peak intensity scaling quadratically as N^2 . The term superfluorescence was later introduced to describe emitters populating an incoherent excited state that must spontaneously synchronize the excited dipoles to build coherence, leading to a time delay between excitation and cooperative emission²⁵. Although the terms SR and SF were initially used interchangeably²⁶, it is now generally accepted that the two phenomena differ in their temporal dynamics and emerge in fundamentally different systems²⁷: an ensemble of N identical units undergoes SR or SF emission depending on the initial dipole alignment and spatial distribution of the emitting units, thus highly ordered and tightly packed units lead to instantaneous SR emission, while larger inter-unit spacing and disorder result in delayed SF emission.

In solid-state systems, cooperativity in the form of SF or SR can be observed when emitters align on a microscopic scale through processes of self-assembly, such as ligand-engineering in quantum dot (QD) ensembles^{1,3,4,28,29} or solvophobic effects in molecular J-aggregates³⁰⁻³⁵. In QD superlattices the degree of cooperativity is limited by the inhomogeneous broadening of

the emitting units and their interunit spacing. QD superlattices with typical spacing of ~ 10 nm were shown to enter the SF regime at cryogenic temperature and high excitation density, displaying redshifted, ultrafast, and delayed bursts of photons with super-Poissonian photon statistics. Nonetheless, their cooperativity remained limited to just a few tens of units³. Shortening of the interunit spacing by ligand design has further led to superradiant emission of temporally correlated photons without time delay at cryogenic temperature²⁹.

Conversely, cooperative systems where emitting units are tightly packed, like molecular J-aggregates with typical interunit distances of ~ 1 -2 nm³⁶, can enter the superradiant regime even at room temperature. Upon aggregation, such systems show the emergence of a J-exciton peak with larger oscillator strength and spectral redshift compared to the monomer, and a characteristic speed-up of the fluorescence decay. These properties have made J-aggregates exceptional materials to investigate strong light-matter interactions and ultrafast energy exchange mechanisms in microcavities and resonant plasmonic systems³⁷⁻⁴¹.

Recent work on bare perovskite films has highlighted the possibility to further enhance cooperativity of SF systems at high temperature by extending electron-phonon coupling through the formation of large polarons⁴²⁻⁴⁵, leading to fast delayed emission with large intensity fluctuations⁴⁶. This is consistent with theoretical predictions of vibrational decoupling of superradiant excitons in optical cavities⁴⁷, where strong coupling with a common, extended optical mode was predicted to reduce the effect of microscale disorder and enable long distance dipole-dipole interaction and macroscopic superradiance⁴⁸⁻⁵⁰.

In this work, we establish that bare J-aggregate films are superradiant and exhibit large photon correlations, hinting at the onset of large-scale interactions between excitons. We then couple superradiant J-excitons to resonant dielectric metasurfaces supporting bound states in the continuum (BIC) modes^{51,52} to extend superradiance beyond the conventional λ^3 limit and

enhance the resulting temporal photon correlations. Experimentally, we observe a pronounced increase in cooperativity, manifested as a speed-up of the photon emission rate, a change in nonlinear scaling of the emission intensity, and photon bunching with excitation density and Rabi splitting. Modelling of the second-order correlation function for interacting J-excitons confirms that the high values of photon bunching observed in our experiments originate from the build-up of macroscopic coherence mediated by the BIC mode and increasing cooperativity up to 250 synchronized J-excitons. These results prove the effectiveness of dielectric metasurfaces as a new open cavity platform to extended cooperativity of superradiant quantum emitters and to generate strongly correlated photons at room temperature.

Emergence of superradiance and photon correlations in bare J-aggregate films

Temporal photon correlations are a distinctive feature of superradiant systems, where bright collective modes with large emission rates are formed by coherent coupling of ordered, tightly packed emitters. When few bright collective modes dominate over dark or low emission rate states, the emitted photons follow a super-Poissonian distribution, leading to strong intensity fluctuations and burst-like photon emission⁷. This phenomenon is quantified by the intensity correlation function, $g^{(2)}(\tau) = \frac{\langle I(t)I(t+\tau) \rangle}{\langle I(t) \rangle^2}$, where large intensity fluctuations associated to bursts of photons typical of cooperative emission lead to photon bunching ($g^{(2)}(0) > 1$).

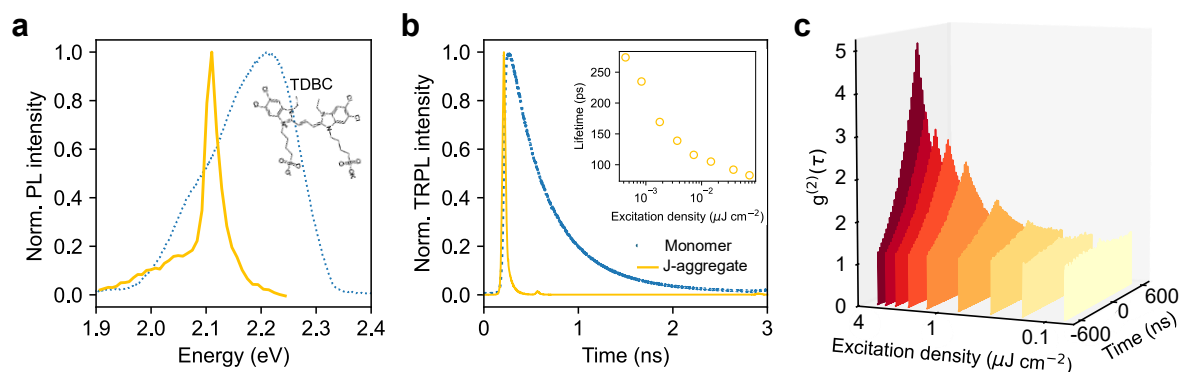


Fig. 1: J-aggregate emission and photon correlations. **a**, Photoluminescence spectra of TDBC monomer (blue dotted line) and J-aggregate (yellow solid line) showing the linewidth narrowing and redshift following aggregation. **b**, Time-resolved photoluminescence measurements of monomer and J-

aggregate displaying the change in lifetime upon aggregation. The inset shows the characteristic lifetime speed-up of superradiance. **c**, Second-order correlation function, $g^{(2)}(\tau)$, measurements as a function of excitation density for the J-aggregate showing $g^{(2)}(0) > 1$ (photon bunching) at all pump powers.

Here, solution grown TDBC J-aggregates were deposited on quartz, yielding $t \sim 25$ nm thick films (Fig. S1a,b), to measure their superradiant signatures and photon correlations. When compared to the monomer, the aggregate emission exhibits a narrow, redshifted J-exciton peak (Fig. 1a), consistent with cooperative coupling among monomeric units. As predicted by Dicke's theory, exciton cooperativity causes a speed-up of fluorescence decay (Fig. 1b), which strongly depends on excitation density (P). At the lowest excitation fluence of $\sim 0.1 \mu\text{J cm}^{-2}$, the J-exciton lifetime ($\tau_J = 274$ ps) reduces to about 5 times that of the monomer film ($\tau_{\text{mon}} = 1480$ ps). At higher excitation fluences, the lifetime reduces further to $\tau_J \sim 83$ ps (inset of Fig. 1b), limited by the temporal resolution of our measuring system. The ratio of monomer (τ_M) to J-aggregate (τ_J) fluorescence lifetime is usually taken as a measure of the average number of coupled units within the aggregate; in our case, this corresponds to $N_{coh} = \frac{\tau_M}{\tau_J} \sim 5-18$ depending on excitation density. A better estimate in the presence of nonradiative components was shown

to be $N_{coh} = \sqrt{\frac{3\pi^2|J|}{W}} - 1$, where W is the J-exciton linewidth and $J = \frac{\lambda_{\text{max}}^J - \lambda_{\text{max}}^{\text{mon}}}{2.4}$ is the dipole-dipole interaction strength⁴⁹. Thus, in TDBC films where luminescence quantum yield is typically low ($\sim 2-5\%$)^{53,54}, $N_{coh} = 10$ units for $W = 0.025$ eV and $|J| = 0.087$ eV. Assuming a slippage spacing of 1.2 nm³⁶, this provides a lower bound for the delocalization of intra-aggregate J-exciton wavefunctions of $\sim 10 \times 1.2 = 12$ nm.

It was recently realized that a universal manifestation of superradiance is the emergence of temporal correlations among the emitted photons, which induce large temporal intensity fluctuations (photon bunching)⁷. To quantify the temporal correlations in the emission of our J-aggregate films, we measured the second order intensity correlation function $g^{(2)}(\tau)$ in a

Hanbury Brown and Twiss interferometer (see Methods). At the lowest excitation density, the films display $g^{(2)}(0) \sim 1.17$ (Fig. 1c). Remarkably, we find that $g^{(2)}(0)$ grows with increasing excitation density, reaching the regime of photon superbunching ($g^{(2)}(0) > 2$) at $P > 1.4 \mu\text{J cm}^{-2}$. This observation cannot be explained by conventional (microscopic) J-aggregate SR where cooperativity is assumed to be limited to just a few coherently coupled monomeric units⁴⁹. Rather, the growth of photon correlations may stem from an increase of stochastic intensity fluctuations, as previously inferred in four-wave mixing experiments in atomic vapours⁵⁵, and chaotic quantum dot microlasers^{56,57}. This can be related to the emergence of macroscopic or inter-aggregate superradiance induced by the large scale coupling of J-excitons, as theoretically predicted for ideal, defect-free, weakly disordered one-dimensional J-aggregates^{47,58}. Of particular interest for the realization of unconventional correlated quantum light sources, the increase of $g^{(2)}(0)$ in J-aggregate films at high fluence is in stark contrast with the reduction of photon correlations typical of parametric sources, where intensity fluctuations are suppressed in the high excitation regime⁵⁹⁻⁶².

In the following, we show that coupling SR emitters to resonant metasurfaces further enhances inter-molecular coupling and unlocks a previously unexplored regime of long-range cooperativity at room temperature, resulting in super-thermal temporal correlations with *massively superbunched* photons ($g^{(2)}(0) \gg 2$).

J-Exciton-Polaritons in BIC metasurfaces

We designed and fabricated metasurfaces consisting of a square lattice of amorphous silicon (*a*-Si) nanopillars that supports C_2 symmetry-protected BIC resonances at the Γ point in the transverse electric (TE) mode. The electric field distribution of the BIC in the x-y and x-z planes is shown in Figs. S2b and S2c, respectively. The metasurfaces were coated with TDBC J-aggregate films with thickness of $t \sim 25$ nm. The geometrical parameters of the metasurfaces

and the organic film thickness were optimized to maximize the spectral overlap between the BIC photonic resonance and the J-exciton energy, at approximately 2.1 eV.

The simulated BIC photonic band of the *a*-Si metasurface shows a typical angular dispersion with quality factor increasing indefinitely (i.e., linewidth narrowing toward zero) toward normal incidence (Fig. 2a), where light cannot couple to the symmetry-protected bound mode (Fig. S2a). This behaviour is consistent with the experimental back focal plane (BFP) TE reflectance map shown in Fig. 2b. The detuning between the photonic mode and the excitonic transition is controlled by varying the nanopillar radius across different metasurfaces to adjust the spectral position of the BIC band - see reflectance maps of Figs. S3a-c and the corresponding spectral linecuts in Fig. 2c ($\theta = 13\text{-}17^\circ$).

In addition to the BIC mode, the metasurface design also supports a higher-energy Mie-type resonance (Fig. 2), whose interactions with dielectric metasurfaces have been investigated in our previous work⁶³.

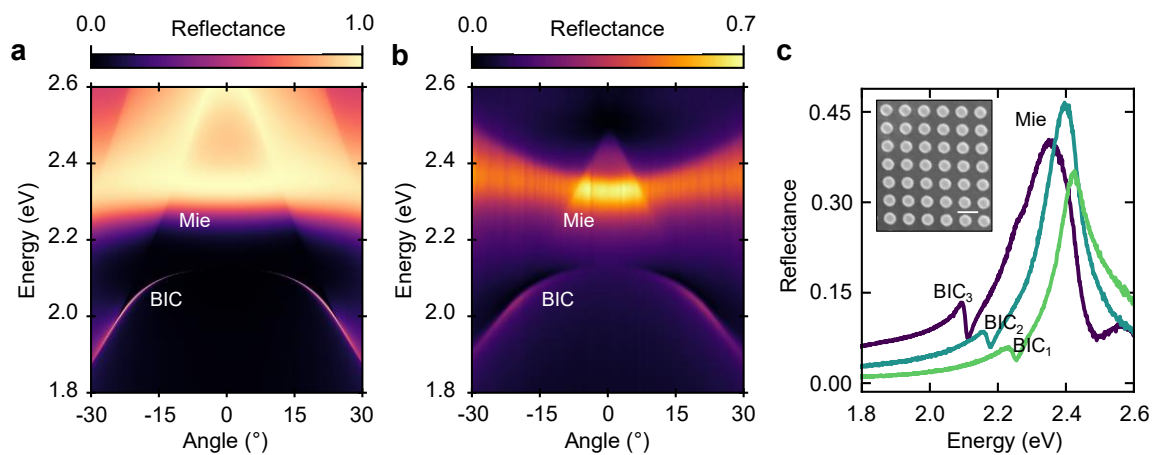


Fig. 1: Bound state in the continuum resonance in a Si metasurface. **a**, RCWA-calculated angle-resolved reflectance map showing the high-Q BIC resonance, characterized by a vanishing linewidth toward normal incidence (angle=0°). **b**, Experimental reflectance measured by angle-resolved back focal plane (BFP) Fourier spectroscopy, confirming the presence of the BIC. **c**, Reflectance spectra

(linecuts of Figs. S3a-c) for metasurfaces with varying nanopillar radii, illustrating the spectral tunability of the BIC resonance. Inset: SEM image of the Si metasurface; the scalebar is 320 nm.

Coating the metasurfaces with the J-aggregate film significantly modifies the photonic band structure, as revealed by the angle-resolved BFP spectral maps for reflectance (Fig. 3a-c) and photoluminescence (Fig. 3d-f). In all cases, a new band emerges below the exciton energy, J_{exc} (indicated by the black dashed lines in Figs. 3a,d), signalling the formation of hybrid light-matter states (exciton-polaritons). Fitting the observed dispersion using a coupled oscillator model⁶⁴, with the Rabi splitting energy $\hbar\Omega$ as the sole fitting parameter, confirms that the new bands correspond to the lower exciton-polariton branches (BIC₁₋₃ LP, shown as white dashed lines). The corresponding upper polariton branches (BIC UP) are not visible due to absorption losses in *a*-Si and TDBC at higher energies. The uncoupled photonic band (BIC_{1,passive}) is also indicated for reference (white dotted line in Fig. 3a). The measured dispersions agree well with full-wave numerical simulations of the coupled system (Fig. S4c).

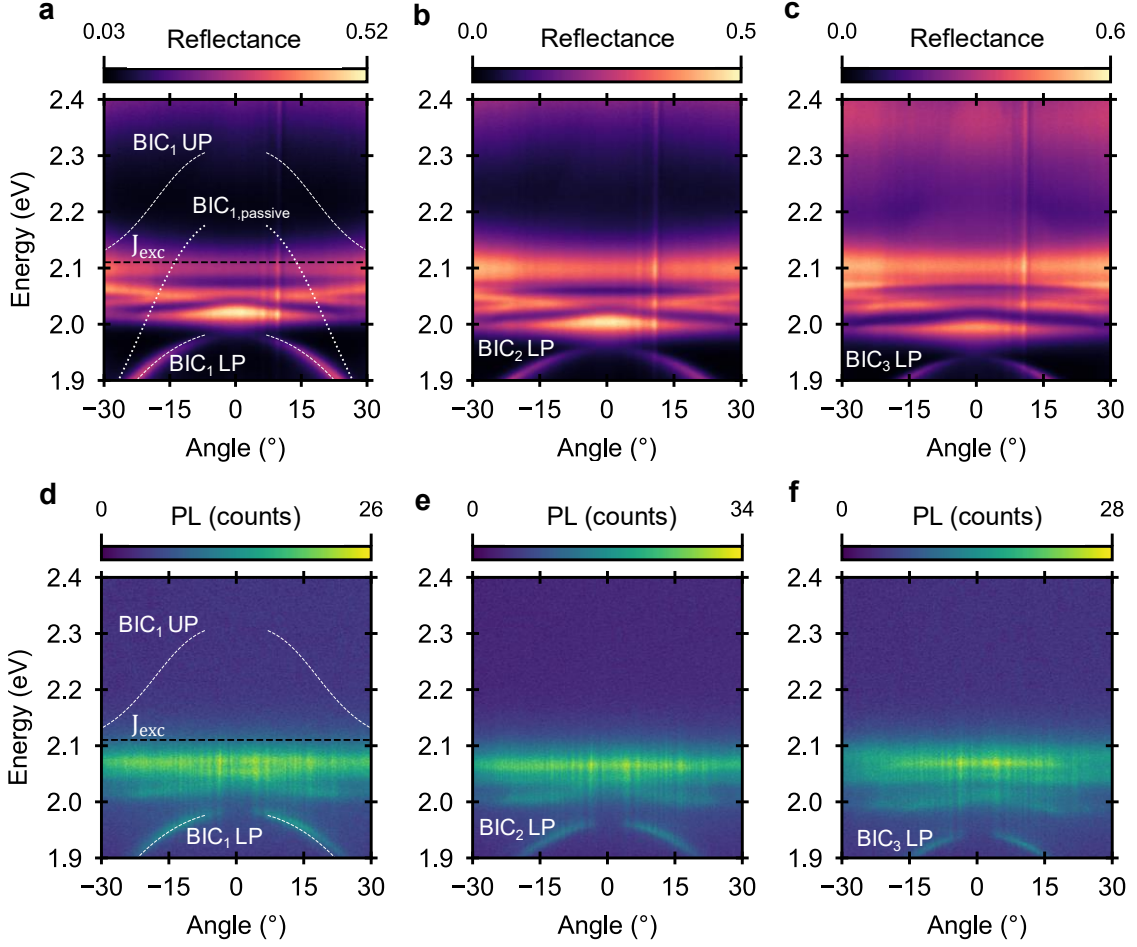


Fig. 2: Strong coupling of the J-exciton with the bound state in the continuum (BIC) resonance. **a–c**, Angle-resolved back focal plane (BFP) reflectance measurements for three metasurfaces with decreasing detuning between the J-exciton (J_{exc} , black dashed line) and photonic BIC, showing the emergence of a lower polariton (LP) branch below the J-exciton energy. The white dotted lines indicate the uncoupled photonic band ($BIC_{1,passive}$), while the white dashed lines correspond to the upper and lower polariton branches obtained from a coupled oscillator model fit. **d–f**, Corresponding angle-resolved photoluminescence (PL) measurements, confirming the formation of the LP branch. The extracted Rabi splitting energies are $\hbar\Omega_{BIC1 LP} = 305$ meV, $\hbar\Omega_{BIC2 LP} = 320$ meV, and $\hbar\Omega_{BIC3 LP} = 328$ meV, with the largest splitting occurring for the metasurface with the smallest detuning from the exciton energy. The upper polariton branch (UP) is not observed due to absorption losses in Si and TDBC at higher energies.

We extract the coupling strength and Rabi splitting for the three metasurfaces/TDBC systems as follows: $g_{0-1} = 160$ meV with $\hbar\Omega_1 = 305$ meV (Fig. 3a,d), $g_{0-2} = 164$ meV with $\hbar\Omega_2 = 320$ meV (Fig. 3b,e), $g_{0-3} = 166$ meV with $\hbar\Omega_3 = 328$ meV (Fig. 3c,f). The largest Rabi splitting is obtained for the sample with the smallest detuning between the photonic mode and the exciton energy. The fact that $g_0 \gg k_B T$ indicates that all three systems are in the strong coupling regime even at room temperature, consistent with the requirement from coupled mode theory⁶⁴, $2g_0 > (\gamma_{\text{exc}} + \gamma_{\text{cav}})/2$, taking the dephasing rate $\gamma_{\text{exc}} \sim 25$ meV measured from J-aggregate film luminescence and the cavity dephasing rate $\gamma_{\text{cav}} \sim 20$ meV predicted from simulations.

Metasurface-enhanced superradiance in the strong coupling regime

Previous studies have shown that local field enhancement shared across spatially separated J-aggregates can overcome local disorder and promote inter-aggregate exciton delocalization³⁰. Here, we exploit the collective and spatially coherent nature of the BIC mode, which extends throughout the entire metasurface⁶⁵ to facilitate coherent coupling between distinct J-aggregate domains.

Steady-state photoluminescence measurements provide the first clear evidence of enhanced cooperativity mediated by the strong light-matter interaction between J-excitons and the BIC mode (Fig. 4). In the coupled systems (Fig. 4b-d), the narrow luminescence peak associated to the LP branch redshifts relative to the bare J-aggregate film emission (Fig. 4a) following the Rabi splitting $\hbar\Omega$ and coupling strength g_0 determined by the metasurface detuning. For the uncoupled J-aggregate film (Fig. 4e), the steady-state PL intensity increases linearly with excitation power, consistent with superradiant emission. This is consistent with the inverse power dependence of the PL lifetime ($\tau \propto 1/P$) and the super-linear scaling of the instantaneous PL peak intensity ($I_l \propto P^n$ with $n > 1$), as detailed in Supplementary Information (see Figs. S5b,c). In contrast, the steady-state PL intensity of the lower polariton

states exhibit a markedly nonlinear response (Fig. 4e-h): the growth of I_{SS} with respect to P can be fitted by a power law $I_{SS} \propto P^n$, with exponents n growing from 1.7 to 2.0 as the Rabi splitting $\hbar\Omega$ increases. This suggests that stronger exciton-cavity coupling is enhancing the superradiant response of the system. Further investigation and modelling of this phenomenon is presented in the following section.

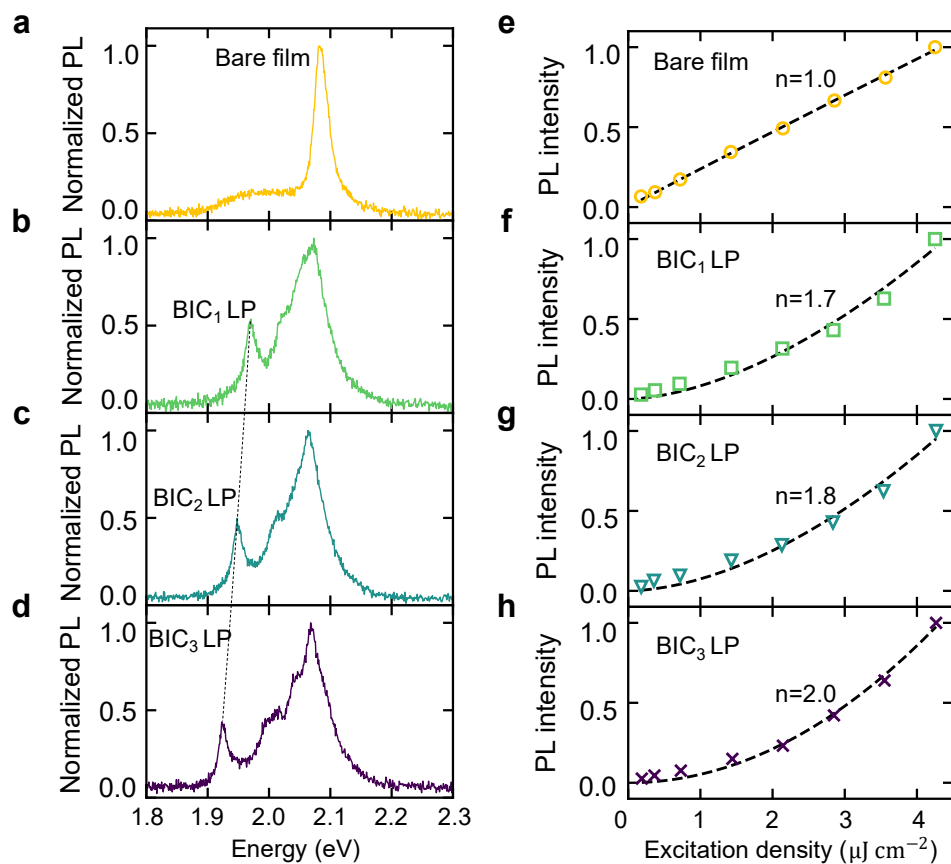


Fig. 3: Superradiant photoluminescence spectra in the strong coupling regime. **a-d**, Steady-state photoluminescence spectra of the J-aggregate film on quartz **(a)** and coupled to the three metasurfaces **(b-d)**, showing a narrow LP peak that redshifts relative to the J_{exc} emission as the Rabi splitting increases. **e-h**, Dependence of the integrated photoluminescence intensity of the J-exciton **(e)** and the lower polariton peak **(f-h)** on excitation density. The J-exciton exhibits a linear dependence, while the

lower polariton exhibits a distinct superlinear growth. The data are fitted with a power law (black dashed lines) with exponent n that increases with Rabi splitting.

Metasurface mediated massive super-bunching

To elucidate how resonant metasurfaces promote coupling between spatially separated superradiant emitters and their effect on temporal correlations, we compare the second-order correlation function of photons emitted by J-excitons in bare films and J-exciton-polaritons in coupled metasurfaces (Fig. 5a). The emission of J-exciton-polaritons shows larger temporal correlations than the bare J-exciton ($g_{LP}^{(2)}(0) > g_{J-exc}^{(2)}(0)$) and systematically increases with coupling strength. $g_{LP}^{(2)}(0)$ grows superlinearly when varying the excitation density (Fig. 5b). For the largest Rabi splitting (BIC₃LP), $g_{LP}^{(2)}(0)$ reaches a maximum value of 13.4, a threefold enhancement over the uncoupled film at the same excitation density. This trend parallels the photoluminescence dependence measured under comparable excitation conditions, consistent with metasurface-enhanced superradiance as the mechanism driving the massively superbunched photon emission regime ($g^{(2)}(0) \gg 2$).

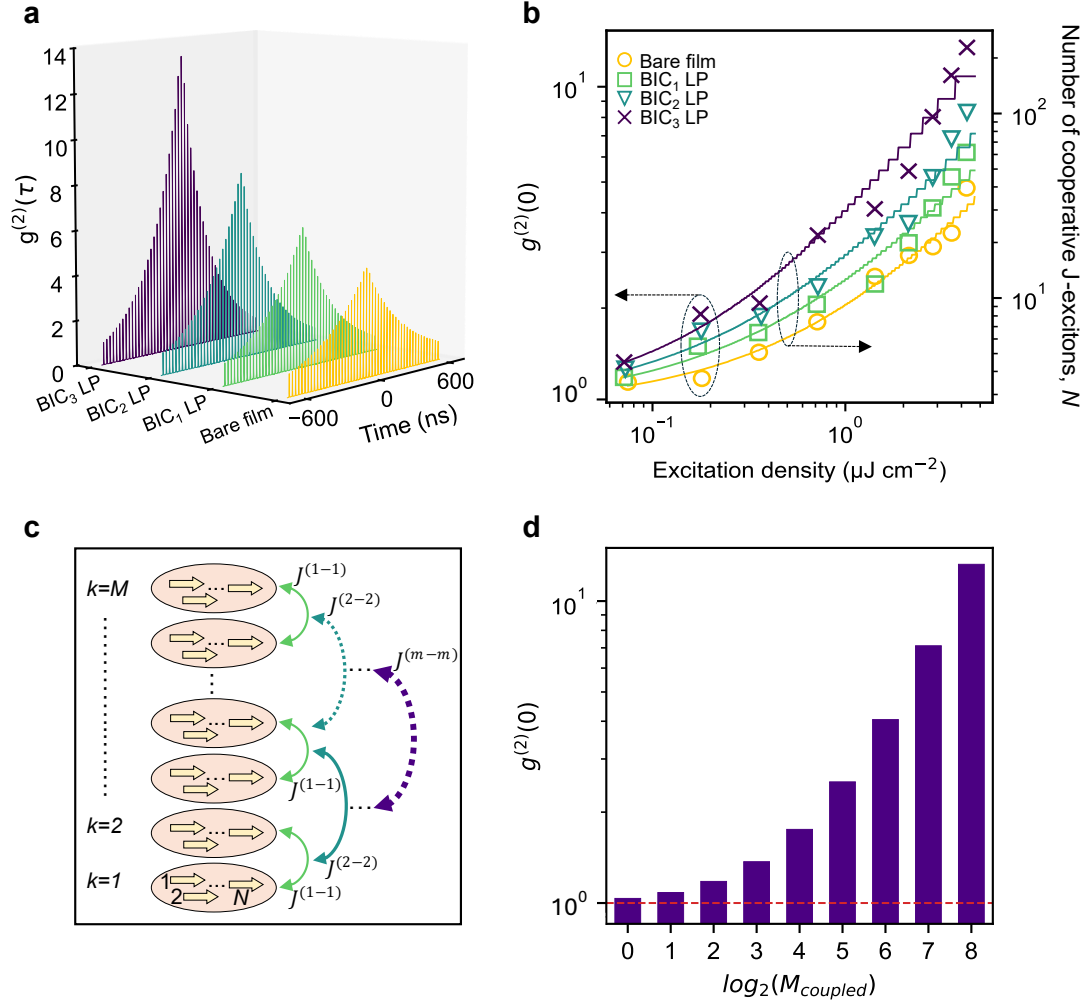


Fig. 5: Inter-aggregate superradiance and super-bunching induced by field enhancement and coupling strength.

a, Experimental second-order correlation function, $g_{(\tau)}^{(2)}$, for the J_{exc} and BIC LP photons at the maximum excitation density, showing increasing photon super-bunching with growing Rabi splitting. The highest Rabi splitting ($\hbar\Omega_{\text{LP-3}} = 328$ meV) corresponds to the highest bunching value of $g_{(\tau=0)}^{(2)} \sim 13.3$. **b**, The experimental zero delay second-order correlation functions, $g_{(\tau=0)}^{(2)}$, demonstrate that photon bunching increases with excitation density, as predicted by the model. The fitting lines represent the modelled results discussed in **c**. **c**, Schematic representation of the model used to describe M J-aggregates each hosting N J-excitons undergoing inter-aggregate interactions of the m order via the inter-aggregate interaction dipole $J^{(m-m)}$. **d**, The model for $g_{(\tau=0)}^{(2)}$ in presence of inter-aggregate coupling predicts its value to grow as the number of coupled J-aggregates (M_{coupled})

increases, with maximal photon bunching observed when all aggregates are coupled (the red dashed line represents $g_{(\tau=0)}^{(2)} = 1$, typical of uncorrelated emission).

To provide a quantitative description of metasurface-mediated inter-aggregate interactions, we developed a model for the second-order correlation function of the photons emitted by M J-aggregates, each hosting N excitons with probability of emission P_{emit} (see Supplementary Information). This description accounts for the presence of multiple delocalized excitons on the same or neighbouring J-aggregate chains^{39,66} and their coherent interactions (Fig. 5c). In such system, $g^{(2)}(0) > 1$ arises from the synchronized emission of multiple excitons mediated by inter-aggregate couplings $J^{(m-m)}$ (interaction order $m = 0, 1, \dots, M$) effectively reducing the number of independent emitters. Assuming a typical quantum yield of 0.02 for TDBC aggregates^{53,54} (P_{emit}) and $N = 4$ (based on measured speed-up of luminescence lifetimes, Fig. S5d), the model predicts increasing $g^{(2)}(0)$ with the number of coupled excitons, reaching $g^{(2)}(0) \approx 13$ for $M_{coupled} = 2^8$ (Fig. 5d). This is in good agreement with $g^{(2)}(0) \approx 13.4$ measured at the maximum excitation fluence of $\sim 4.3 \mu\text{J cm}^{-2}$. For comparison, the behaviour expected for completely uncorrelated emitters ($g^{(2)}(0) \rightarrow 1$) is shown by the dashed red line in Fig. 5d.

It is worth noting that the massively superbunched photon emission regime can only be achieved starting with sub-unity quantum yield of uncoupled J-excitons (Fig. S7). This is because high $g^{(2)}(0)$ values correspond to large temporal intensity fluctuations, originating from partially emissive superradiant ensembles. By contrast, a deterministic superradiant source with unitary quantum yield would emit a fixed number of photons per pulse, resulting in a uniform temporal photon distribution, e.g. $g^{(2)}(0) = 1$, regardless of the number of coupled emitters. Similar behaviour is displayed by parametric single-photon sources, where

pumping power increases the quantum yield of multiphoton events, eventually reducing photon bunching^{67,68}.

The number of coupled emitters predicted by the model for different $g^{(2)}(0)$ can be used to evaluate the increase of inter-aggregate cooperativity as a function of excitation density. We consider a total of $M = 2^{10}$ J-excitons being excited in a $t \times \lambda^2$ volume (based on the number of absorbed photons in the experiment, see Supporting information) and compute photon bunching for each interaction order and excitation density to obtain the solid lines in Fig. 5b. The calculated values are in good agreement with the experimental data, proving the role of inter-aggregate coupling in shaping temporal correlations. We estimate a maximum of $N_{J-exc} = 73$ coherently interacting excitons in the bare film at the highest excitation density, compared to $N_{BIC3LP} = 256$ coherently emitting exciton-polaritons in the metasurface exhibiting the largest Rabi splitting. This 3.5-fold increase in the number of interacting J-excitons demonstrates the potential of common-mode coupling in resonant metasurfaces to realize sources with massively superbunched photon emission.

Discussion and conclusions

We demonstrated that dielectric metasurfaces supporting bound-state-in-the-continuum resonances can enhance superradiance by strongly coupling to J-excitons. Large temporal correlations displayed by bare J-aggregate films at room temperature can be further enhanced by promoting inter-aggregate interactions through the common BIC mode, inducing superlinear scaling of steady-state emission and photon superbunching with excitation density. The relation between inter-aggregate coupling and the growth of temporal correlations with pump power is confirmed by modelling the second-order correlation function for interacting J-excitons. Experimentally, we observe a transition to the regime of massively superbunched

photon emission by varying the pump power, achieving $g^{(2)}(0) \sim 13.4$ at the maximum coupling strength (Rabi splitting) and excitation density investigated.

These findings could be applied in areas that demand highly correlated photon sources such as secure quantum communication and correlated classical or quantum imaging. For instance, emergent thermal QKD schemes^{22,23} rely on thermal light intensity fluctuations to encode information and achieve high transfer rates are limited by the thermal nature of light ($g^{(2)}(0) = 2$). Our system could help improve information transfer rates and potentially enhance security by providing tunable intensity fluctuations through the power dependence of $g^{(2)}(0)$. Other opportunities may lie in the enhancement of nonlinear optical effects in the low excitation regime, such as two-photon absorption^{10,11} or higher-order harmonic generation¹⁶⁻¹⁸. Nonlinear processes require multiple photons to interact simultaneously within a nonlinear medium, an intrinsically inefficient process that scales superlinearly with power and can quickly reach damaging thresholds. At a given input power, strongly correlated sources increase the yield of nonlinear processes, reducing the required illumination intensity. This is particularly advantageous for applications such as high-contrast two-photon excited fluorescence imaging of sensitive biological samples residing in noisy environments^{12,14}. Finally, there may be further applications in imaging and ranging, including correlated imaging^{12,13,15}, ghost imaging^{8,9}, and LiDAR¹⁹. Since the detection probability of correlated events determines the signal to noise ratio, highly correlated sources may yield faster acquisitions and better visibility.

Methods

Metasurface design

The bound state in the continuum supporting metasurface was designed via Finite Difference Time Domain (FDTD) and Rigorous Coupled-Wave Analysis (RCWA) suit of the commercial software Ansys Lumerical. The nanoresonators geometry supports an out-of-plane magnetic dipole resonance that cannot couple to an incoming transverse electric excitation at normal incidence, giving rise to a symmetry-protected BIC at $\theta = 0^\circ$. Comsol Multiphysics eigenfrequency solver is instead utilized to calculate the quality factor of the BIC as a function of incident angle (Fig. S2a).

Metasurface fabrication

Quartz substrates were cleaned by sequential sonication in solvents: AR 600-71 (Allresist), acetone and IPA. The substrates were then dried with nitrogen and underwent a short oxygen plasma treatment. Undoped amorphous Si layer was grown using a plasma enhanced chemical vapor deposition system (Cello Aegis-20) at 200°C. 50 μm x 50 μm BIC metamaterial arrays were defined using e-beam lithography with AR-N 7520 resist and Electra 92 conductive coating (Allresist), followed by inductively coupled plasma reactive ion etching of Si with SF₆/O₂ (Oxford PlasmaPro100 ICP-RIE system). The remaining resist was removed by sequential soaking the sample in solvents: AR 300-76 (Allresist), AR 600-71, acetone and IPA. The samples were then dried with nitrogen, followed by a short oxygen plasma treatment.

Processing and deposition of TDBC J-aggregates

The cyanine dye 5,6-Dichloro-2-[[5,6-dichloro-1-ethyl-3-(4-sulfobutyl)-benzimidazol-2-ylidene]-propenyl]-1-ethyl-3-(4-sulfobutyl)-benzimidazolium hydroxide, inner salt, sodium salt J-aggregate (TDBC) was purchased from Biosynth Carbosynth (CAS: 18462-64-1) and was dissolved in de-ionized water with a concentration of 20 $\frac{\text{mg}}{\text{mL}}$. The solution was left in the

dark for 3 days to form J-aggregates. 100 μL of the solution were then deposited by spincoating at 4000 rpm for 60 seconds on the fabricated Si metasurfaces. The sample was then dried with N_2 .

Angle-resolved spectroscopy

Angle-resolved reflectance (ARR) and photoluminescence (ARPL) measurements were performed with a custom built microspectrometer setup consisting of an inverted optical microscope (Nikon Ti-u, 50x objective, $\text{NA} = 0.55$), a spectrograph (Andor SR-303i with a 300 lines/mm grating), and a charged-coupled detector (CCD, Andor iDus 420). A series of lenses along the beam path between the microscope and the spectrograph projects the back focal plane (BFP) of the collection objective on the slit of the spectrograph, allowing the collection of angular information within bounds defined by $\frac{k_x}{k_0} = \text{NA} = 0.55$. The sample was excited via a halogen lamp for ARR measurements, while a 405 nm continuous wave laser was used for ARPL measurements.

Photoluminescence and photon correlation spectroscopy

Steady-state, time-resolved, and photon correlation measurements are performed by exciting the sample with a 405 nm picosecond pulsed laser with 40 MHz repetition rate (PicoQuant PDL 800-D). The emission of the sample is collected via a 100x magnification 0.9 NA microscope objective and is spectrally filtered by interchangeable bandpass filters. A dichroic mirror and a longpass filter are utilized to remove the reflected and scattered laser beam. After filtering, the emission can be redirected to a spectrometer or a laser-synched time controller (PicoHarp 300) via fibers, to perform steady-state or time-resolved and photon correlation measurements, respectively.

The photon statistics discussed in the manuscript are measured in a standard Hanbury-Brown-Twiss (HBT) interferometer. The emission of the sample is collected via a microscope objective

and is re-directed to a 50/50 fiber beam splitter connected to two avalanche photodetectors (Excelitas SPCM-AQRH-14-FC, APD 1 and APD 2) for single-photon counting. A time controller (ID Quantique ID900) tags the photon events collected by the detectors and builds the second order correlation function, $g^{(2)}(\tau)$, based on the number of coincidences and the arrival times of the photons. The resulting $g^{(2)}(\tau)$ is normalized by dividing by the coincidences at large temporal delays, where emission is uncorrelated.

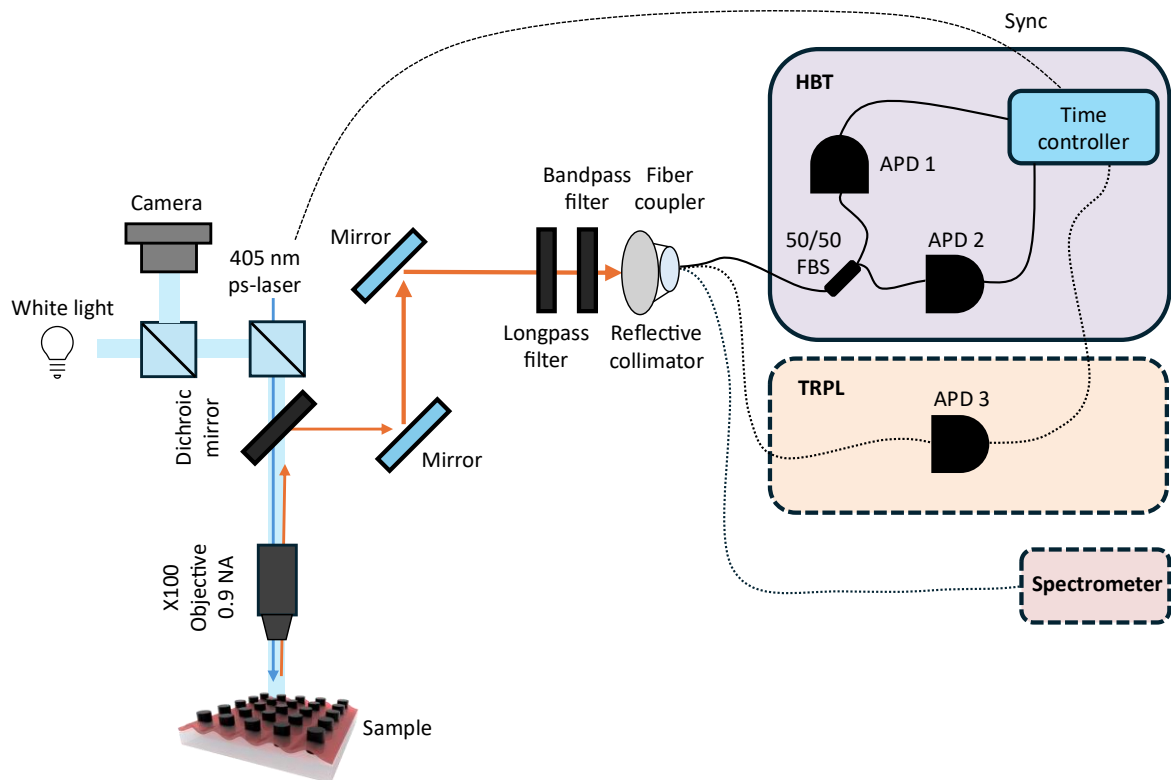


Fig. S6: Photoluminescence characterization setup Schematic of the setup utilized for the characterization of the photoluminescence intensity, lifetime, and photon correlations. The collection path can be redirected via optical fibers to a spectrometer for PL spectral measurements, a time-controller for time-resolved measurements (TRPL), or to a Hanbury-Brown-Twiss setup (HBT) for photon correlation measurements.

Author contributions

M.M. G.A. and C.S. conceived the idea. M.M. performed all spectroscopy measurements and analysed the data with the help of G.A.. A.M.D. carried out design optimisation and fabrication of the silicon metasurfaces. A.N.V. modelled the superradiant emission from interacting J-aggregates and their second order correlation function. M.M. and G.A. drafted the manuscript, with all authors contributing to editing and review. C.S. supervised the work.

Acknowledgements

Research was supported by the Singapore Ministry of Education, (Grant no. MOE-T2EP50222-0015) and by the Singapore's National Research Foundation through the National Centre for Integrated Photonics (Grant no. NRF-MSG-2023-0002). The authors would like to acknowledge and thank the Nanyang NanoFabrication Centre (N2FC).

References

1. Rainò, G., Utzat, H., Bawendi, M. G. & Kovalenko, M. V. Superradiant emission from self-assembled light emitters: From molecules to quantum dots. *MRS Bull.* **45**, 841–848 (2020).
2. Song, Y. *et al.* On-demand manipulation of superbunching emission from colloidal quantum dots and its application in noise-resistance correlated biphoton imaging. Preprint at <https://doi.org/10.48550/arXiv.2503.12384> (2025).
3. Rainò, G. *et al.* Superfluorescence from lead halide perovskite quantum dot superlattices. *Nature* **563**, 671–675 (2018).
4. Scheibner, M. *et al.* Superradiance of quantum dots. *Nat. Phys.* **3**, 106–110 (2007).
5. Temnov, V. V. & Woggon, U. Photon statistics in the cooperative spontaneous emission. *Opt. Express* **17**, 5774–5782 (2009).
6. Jahnke, F. *et al.* Giant photon bunching, superradiant pulse emission and excitation trapping in quantum-dot nanolasers. *Nat. Commun.* **7**, 11540 (2016).
7. Masson, S. J. & Asenjo-Garcia, A. Universality of Dicke superradiance in arrays of quantum emitters. *Nat. Commun.* **13**, 2285 (2022).
8. Zhu, X.-H. *et al.* High-Resolution Microscopic Ghost Imaging for Bioimaging. *Phys. Rev. Appl.* **20**, 014028 (2023).
9. Eshun, A. *et al.* 3D quantum ghost imaging microscope. *Optica* **12**, 1109–1112 (2025).
10. Jechow, A., Seefeldt, M., Kurzke, H., Heuer, A. & Menzel, R. Enhanced two-photon excited fluorescence from imaging agents using true thermal light. *Nat. Photonics* **7**, 973–976 (2013).
11. Schlawin, F., Dorfman, K. E. & Mukamel, S. Entangled Two-Photon Absorption Spectroscopy. *Acc. Chem. Res.* **51**, 2207–2214 (2018).
12. Varnavski, O. & Goodson, T. I. Two-Photon Fluorescence Microscopy at Extremely Low Excitation Intensity: The Power of Quantum Correlations. *J. Am. Chem. Soc.* **142**, 12966–12975 (2020).
13. Lubin, G., Oron, D., Rossman, U., Tenne, R. & Yallapragada, V. J. Photon Correlations in Spectroscopy and Microscopy. *ACS Photonics* **9**, 2891–2904 (2022).
14. Luu, P., Fraser, S. E. & Schneider, F. More than double the fun with two-photon excitation microscopy. *Commun. Biol.* **7**, 364 (2024).
15. Tsao, C. *et al.* Enhancing spectroscopy and microscopy with emerging methods in photon correlation and quantum illumination. *Nat. Nanotechnol.* **20**, 1001–1016 (2025).
16. Qu, Y. & Singh, S. Photon correlation effects in second harmonic generation. *Opt. Commun.* **90**, 111–114 (1992).
17. Spasibko, K. Yu. *et al.* Multiphoton Effects Enhanced due to Ultrafast Photon-Number Fluctuations. *Phys. Rev. Lett.* **119**, 223603 (2017).
18. Rasputnyi, A. *et al.* High-harmonic generation by a bright squeezed vacuum. *Nat. Phys.* **20**, 1960–1965 (2024).
19. Tan, P. K., Yeo, X. J., Leow, A. Z. W., Shen, L. & Kurtsiefer, C. Practical Range Sensing with Thermal Light. *Phys. Rev. Appl.* **20**, 014060 (2023).
20. Jennewein, T., Simon, C., Weihs, G., Weinfurter, H. & Zeilinger, A. Quantum Cryptography with Entangled Photons. *Phys. Rev. Lett.* **84**, 4729–4732 (2000).
21. Dynes, J. F. *et al.* Testing the photon-number statistics of a quantum key distribution light source. *Opt. Express* **26**, 22733–22749 (2018).
22. Newton, E., Ghesquière, A., Wilson, F. L., Varcoe, B. T. H. & Moseley, M. Quantum secrecy in thermal states. *J. Phys. B At. Mol. Opt. Phys.* **52**, 125501 (2019).
23. Walton, A., Ghesquière, A. & Varcoe, B. T. H. Quantum Key Distribution with Displaced Thermal States. *Entropy* **26**, 488 (2024).
24. Dicke, R. H. Coherence in Spontaneous Radiation Processes. *Phys. Rev.* **93**, 99–110 (1954).
25. Bonifacio, R. & Lugiato, L. A. Cooperative radiation processes in two-level systems: Superfluorescence. *Phys. Rev. A* **11**, 1507–1521 (1975).
26. Gross, M. & Haroche, S. Superradiance: An essay on the theory of collective spontaneous emission. *Phys. Rep.* **93**, 301–396 (1982).
27. Russ, B. & Eisler, C. N. The future of quantum technologies: superfluorescence from solution-processed, tunable materials. *Nanophotonics* **13**, 1943–1951 (2024).

28. Zhu, C. *et al.* Single-photon superradiance in individual caesium lead halide quantum dots. *Nature* **626**, 535–541 (2024).
29. Luo, L. *et al.* Polarized Superradiance from CsPbBr₃ Quantum Dot Superlattice with Controlled Interdot Electronic Coupling. *Nano Lett.* **25**, 6176–6183 (2025).
30. Quenzel, T. *et al.* Plasmon-Enhanced Exciton Delocalization in Squaraine-Type Molecular Aggregates. *ACS Nano* **16**, 4693–4704 (2022).
31. Fidler, H., Knoester, J. & Wiersma, D. A. Superradiant emission and optical dephasing in J-aggregates. *Chem. Phys. Lett.* **171**, 529–536 (1990).
32. De Rossi, U., Daehne, S. & Lindrum, M. Increased Coupling Size in J-Aggregates through N-n-Alkyl Betaine Surfactants. *Langmuir* **12**, 1159–1165 (1996).
33. Minoshima, K., Taiji, M., Misawa, K. & Kobayashi, T. Femtosecond nonlinear optical dynamics of excitons in J-aggregates. *Chem. Phys. Lett.* **218**, 67–72 (1994).
34. Würthner, F., Kaiser, T. E. & Saha-Möllner, C. R. J-Aggregates: From Serendipitous Discovery to Supramolecular Engineering of Functional Dye Materials. *Angew. Chem. Int. Ed.* **50**, 3376–3410 (2011).
35. Jelley, E. E. Spectral Absorption and Fluorescence of Dyes in the Molecular State. *Nature* **138**, 1009–1010 (1936).
36. Thanippuli Arachchi, D. H. *et al.* Bright and Fast Emission from Robust Supramolecular J-Aggregate Nanostructures through Silica-Encapsulation. *ACS Nano* **18**, 20422–20434 (2024).
37. Vasa, P. *et al.* Real-time observation of ultrafast Rabi oscillations between excitons and plasmons in metal nanostructures with J-aggregates. *Nat. Photonics* **7**, 128–132 (2013).
38. Mewes, L., Wang, M., Ingle, R. A., Börjesson, K. & Chergui, M. Energy relaxation pathways between light-matter states revealed by coherent two-dimensional spectroscopy. *Commun. Phys.* **3**, 157 (2020).
39. Quenzel, T. *et al.* Plasmon-Enhanced Exciton Delocalization in Squaraine-Type Molecular Aggregates. *ACS Nano* **16**, 4693–4704 (2022).
40. Russo, M. *et al.* Direct Evidence of Ultrafast Energy Delocalization Between Optically Hybridized J-Aggregates in a Strongly Coupled Microcavity. *Adv. Opt. Mater.* **12**, 2400821 (2024).
41. Zhao, X. *et al.* Monolayer J-Aggregate Crystals Strong Coupling with an All-Dielectric Metasurface for Photonic Properties Modification. *Laser Photonics Rev.* **n/a**, e01208.
42. Miyata, K. *et al.* Large polarons in lead halide perovskites. *Sci. Adv.* **3**, e1701217 (2017).
43. Wong, W. P. D. *et al.* Large Polaron Self-Trapped States in Three-Dimensional Metal-Halide Perovskites. *ACS Mater. Lett.* **2**, 20–27 (2020).
44. Srimath Kandada, A. R. & Silva, C. Exciton Polarons in Two-Dimensional Hybrid Metal-Halide Perovskites. *J. Phys. Chem. Lett.* **11**, 3173–3184 (2020).
45. Jin, Z. *et al.* Photoinduced large polaron transport and dynamics in organic–inorganic hybrid lead halide perovskite with terahertz probes. *Light Sci. Appl.* **11**, 209 (2022).
46. Biliroglu, M. *et al.* Unconventional solitonic high-temperature superfluorescence from perovskites. *Nature* **642**, 71–77 (2025).
47. Spano, F. C. Optical microcavities enhance the exciton coherence length and eliminate vibronic coupling in J-aggregates. *J. Chem. Phys.* **142**, 184707 (2015).
48. Bricks, J. L., Slominskii, Y. L., Panas, I. D. & Demchenko, A. P. Fluorescent J-aggregates of cyanine dyes: basic research and applications review. *Methods Appl. Fluoresc.* **6**, 012001 (2017).
49. Jumbo-Nogales, A. *et al.* Cross Determination of Exciton Coherence Length in J-Aggregates. *J. Phys. Chem. Lett.* **13**, 10198–10206 (2022).
50. Mello, O. *et al.* Extended many-body superradiance in diamond epsilon near-zero metamaterials. *Appl. Phys. Lett.* **120**, (2022).
51. Hsu, C. W., Zhen, B., Stone, A. D., Joannopoulos, J. D. & Soljačić, M. Bound states in the continuum. *Nat. Rev. Mater.* **1**, 16048 (2016).
52. Azzam, S. I. & Kildishev, A. V. Photonic Bound States in the Continuum: From Basics to Applications. *Adv. Opt. Mater.* **9**, 2001469 (2021).
53. Sorokin, A. V. *et al.* Exciton Dynamics and Self-Trapping of Carbocyanine J-Aggregates in Polymer Films. *J. Phys. Chem. C* **123**, 9428–9444 (2019).

54. Anantharaman, S. B., Stöferle, T., Nüesch, F. A., Mahrt, R. F. & Heier, J. Exciton Dynamics and Effects of Structural Order in Morphology-Controlled J-Aggregate Assemblies. *Adv. Funct. Mater.* **29**, 1806997 (2019).
55. Zhang, S. *et al.* Controllable superbunching effect from four-wave mixing process in atomic vapor. *Opt. Express* **28**, 21489–21498 (2020).
56. Albert, F. *et al.* Observing chaos for quantum-dot microlasers with external feedback. *Nat. Commun.* **2**, 366 (2011).
57. Redlich, C. *et al.* Mode-switching induced super-thermal bunching in quantum-dot microlasers. *New J. Phys.* **18**, 063011 (2016).
58. Spano, F. C. & Mukamel, S. Superradiance in molecular aggregates. *J. Chem. Phys.* **91**, 683–700 (1989).
59. Qiang, G. *et al.* Giant Superbunching Emission from Mesoscopic Perovskite Emitter Clusters. *Adv. Opt. Mater.* **12**, (2023).
60. Fiedler, S. *et al.* Sub-to-super-Poissonian photon statistics in cathodoluminescence of color center ensembles in isolated diamond crystals. *Nanophotonics* **12**, 2231–2237 (2023).
61. Fiedler, S. *et al.* Photon superbunching in cathodoluminescence of excitons in WS₂ monolayer. *2D Mater.* **10**, 021002 (2023).
62. Meuret, S. Photon Bunching in Cathodoluminescence. *Phys. Rev. Lett.* **114**, (2015).
63. Marangi, M. *et al.* Enhancing cooperativity of molecular J-aggregates by resonantly coupled dielectric metasurfaces. *Nanophotonics* **13**, 3519–3526 (2024).
64. Zhang, L., Gogna, R., Burg, W., Tutuc, E. & Deng, H. Photonic-crystal exciton-polaritons in monolayer semiconductors. *Nat. Commun.* **9**, 713 (2018).
65. Dong, Z. *et al.* Nanoscale mapping of optically inaccessible bound-states-in-the-continuum. *Light Sci. Appl.* **11**, 20 (2022).
66. Mok, W.-K., Asenjo-Garcia, A., Sum, T. C. & Kwek, L.-C. Dicke Superradiance Requires Interactions beyond Nearest Neighbors. *Phys. Rev. Lett.* **130**, 213605 (2023).
67. Feng, J. *et al.* Polarization-entangled photon-pair source with van der Waals 3R-WS₂ crystal. *eLight* **4**, 16 (2024).
68. Henry, A. *et al.* Correlated twin-photon generation in a silicon nitride loaded thin film PPLN waveguide. *Opt. Express* **31**, 7277–7289 (2023).
69. Murai, S. *et al.* Bound States in the Continuum in the Visible Emerging from out-of-Plane Magnetic Dipoles. *ACS Photonics* **7**, 2204–2210 (2020).
70. Anantharaman, S. B. *et al.* Enhanced Room-Temperature Photoluminescence Quantum Yield in Morphology Controlled J-Aggregates. *Adv. Sci.* **8**, 1903080 (2021).
71. Lindrum, M., Glismann, A., Moll, J. & Daehne, S. Fluorescence lifetime measurements and hole-burning experiments on J-aggregates of a benzimidocarbocyanine dye. *Chem. Phys.* **178**, 423–432 (1993).
72. Observation of transition from superfluorescence to polariton condensation in CsPbBr₃ quantum dots film | Light: Science & Applications. https://www.nature.com/articles/s41377-024-01378-5?error=cookies_not_supported&code=eaa58a56-cdcb-43a2-a323-672e08f9ce86#Sec8.
73. Stryzhenko, S., Bruns, A. & Peters, T. π scaling of large-sample collective decay in inhomogeneous ensembles. *Phys. Rev. Res.* **6**, 013091 (2024).
74. Pozina, G. *et al.* Super-radiant mode in InAs—monolayer—based Bragg structures. *Sci. Rep.* **5**, 14911 (2015).
75. Huang, K. *et al.* Room-temperature upconverted superfluorescence. *Nat. Photonics* **16**, 737–742 (2022).
76. Ultrafast upconversion superfluorescence with a sub-2.5 ns lifetime at room temperature | Nature Communications. <https://www.nature.com/articles/s41467-024-54314-x>.
77. Frolov, S. V., Gellermann, W., Ozaki, M., Yoshino, K. & Vardeny, Z. V. Cooperative Emission in π -Conjugated Polymer Thin Films. *Phys. Rev. Lett.* **78**, 729–732 (1997).
78. Miyajima, K., Kumagai, Y. & Ishikawa, A. Ultrashort Radiation of Biexcitonic Superfluorescence from High-Density Assembly of Semiconductor Quantum Dots. *J. Phys. Chem. C* **121**, 27751–27757 (2017).

79. Findik, G. *et al.* High-temperature superfluorescence in methyl ammonium lead iodide. *Nat. Photonics* **15**, 676–680 (2021).
80. Biliroglu, M. *et al.* Room-temperature superfluorescence in hybrid perovskites and its origins. *Nat. Photonics* **16**, (2022).
81. Haider, G. *et al.* Superradiant Emission from Coherent Excitons in van Der Waals Heterostructures. *Adv. Funct. Mater.* **31**, 2102196 (2021).
82. Lupton, J. M. & Vogelsang, J. Photon correlations probe the quantized nature of light emission from optoelectronic materials. *Appl. Phys. Rev.* **8**, 041302 (2021).
83. Manceau, M. *et al.* CdSe/CdS Dot-in-Rods Nanocrystals Fast Blinking Dynamics. *ChemPhysChem* **19**, 3288–3295 (2018).

Supplementary information

J-aggregate film characterization

The J-aggregate film roughness and thickness is characterized by atomic force microscopy (AFM). The film has an absolute roughness of 3.15 nm and a thickness of 25 nm after spincoating on glass substrates (Fig. S1a-c). The refractive index of the film is characterized via ellipsometry and is shown in Fig. S1d. The complex index is utilised in the RCWA simulations to calculate the photonic band dispersion of the *active* structure.

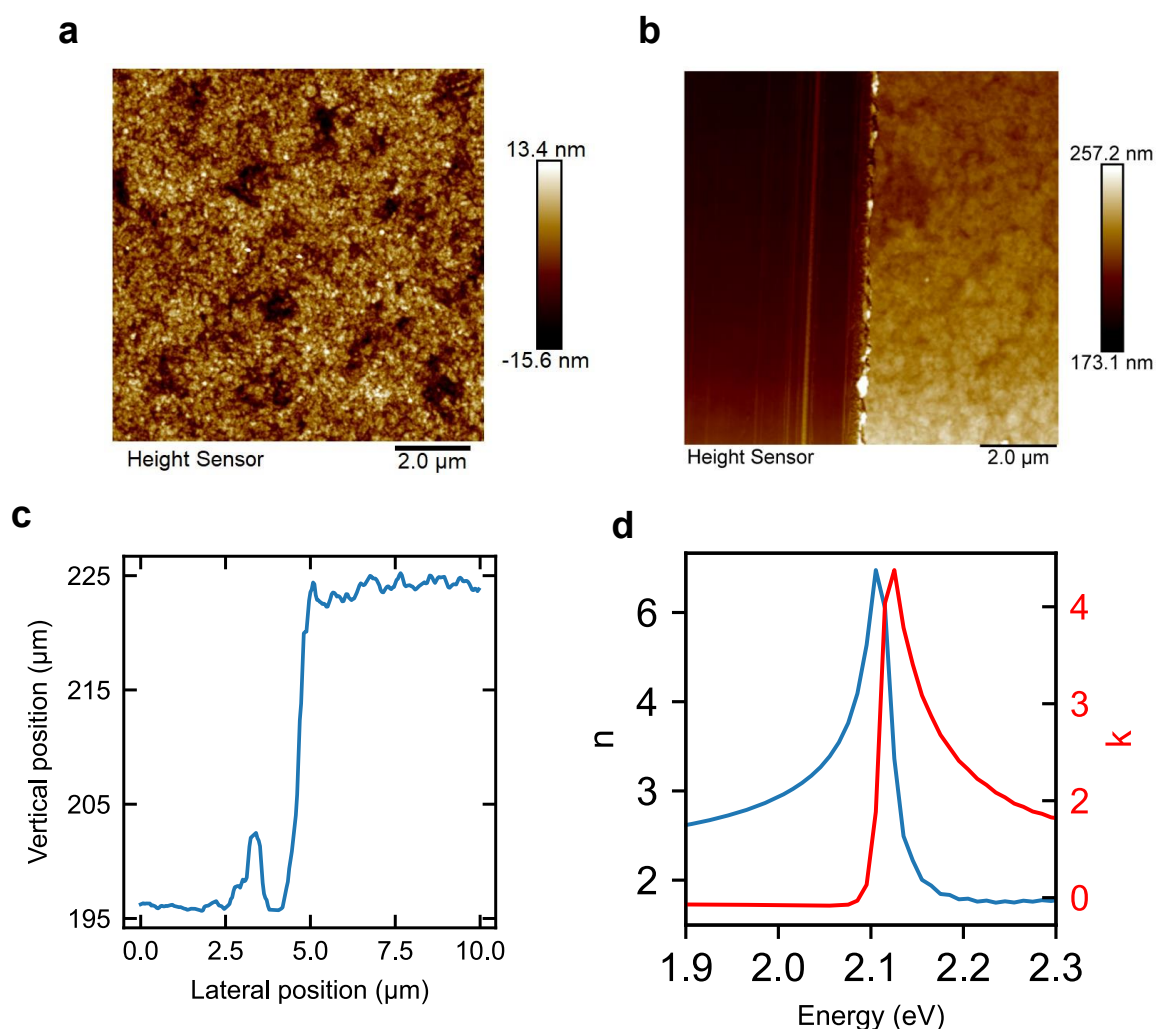


Fig. S1: Bare J-aggregate film characterization a, AFM surface scan of a J-aggregate film with an absolute roughness of 3.15 nm. b, AFM surface scan of a J-aggregate film around a cut

made with a syringe tip to characterize the film thickness. **c**, Profile measurement along an horizontal cut of **b**, revealing a J-aggregate film thickness of 25 nm. **d**, Measured refractive index of the J-aggregate film.

Bound state in the continuum resonance in Silicon metasurface

The silicon metasurfaces supports a 2-fold rotational (C_2) symmetry-protected BIC, arising from an out-of-plane magnetic dipole (MD), generated by displacement currents around the normal direction. Away from the normal direction, the bound states become leaky with finite quality factors as reported in Fig. S2a. The electric field distribution of the mode is shown in Fig S2b and S2c, depicting large field enhancements in proximity to the TDBC film and a null electric field at normal incidence as expected of BICs.

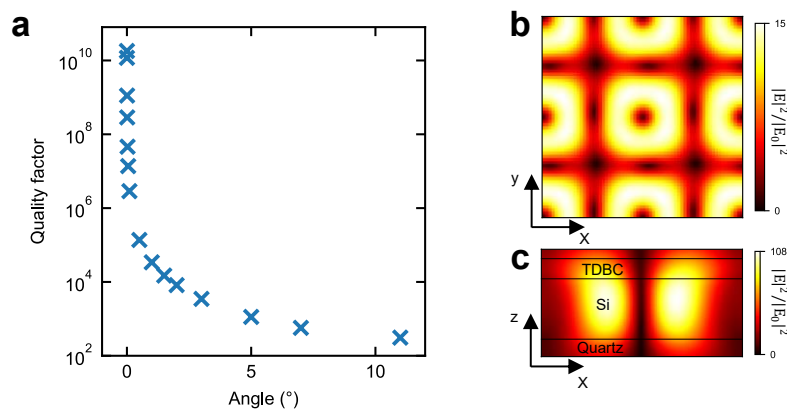


Fig. S2: Quality factor and field enhancement of the bound state in the continuum (BIC) resonance

a, Quality factor of the BIC as a function of angle, shown to increase exponentially as the resonance approaches the normal direction (0°). **b** and **c**, Normalized electric field magnitude spatial distribution in a horizontal (**b**) and (**c**) vertical cross section showing large field enhancement in proximity to the TDBC film. The horizontal cross section is taken in the middle of the TDBC film in the x-y plane, while the vertical cross section is taken at the centre of the unit cell cutting the Si nanopillar in half along the x-z plane.

The experimental photonic dispersion of the metasurfaces discussed in the main text are shown in Fig. S3a-c where the BIC appears as a Fano-shaped peak in reflectance with vanishing linewidth as the dispersion approaches the symmetry-protected normal incidence. The BIC resonance is redshifted by increasing the radius of the nanopillars between 72 to 78 nm (as reproduced by RCWA simulations shown in Fig. S4a and Fig. 2a), while the unit cell period is kept constant at 315 nm. The BIC appears more defined as the radius increases due to its spectral position approaching a spectral range where silicon has lower losses, in accordance to the results reported in [69].

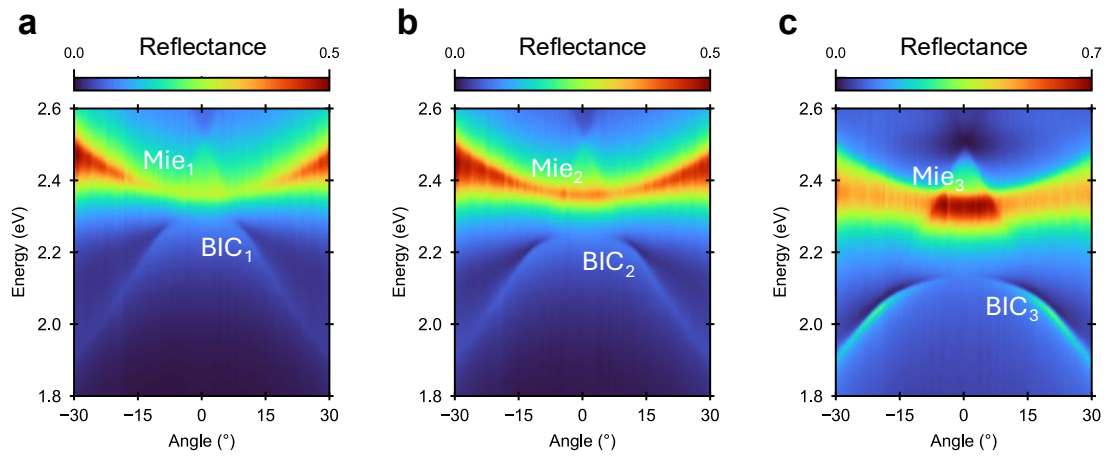


Fig. S3: Experimental photonic dispersion of the bare BIC a-c, Experimental angle-resolved reflectance of the bare metasurfaces showing the typical BIC dispersion for increasing radii of the nanopillars.

Strong coupling regime

In order to confirm that the *active* system is in the strong coupling regime a coupled oscillator model is utilized to model the J-exciton and the cavity resonance as two interacting harmonic oscillators that give rise to the upper and lower exciton-polariton branches. In this framework, the J-exciton is modelled as an oscillator with fixed, dispersion-less, resonance energy $E_{exc} =$

2.11 eV and losses defined by its linewidth $\gamma_{exc}=0.028$ eV. While the BIC cavity resonance energy E_{cav} and losses γ_{cav} are both highly dispersive as shown in the photonic dispersion in Fig. 2a. Furthermore, the photonic dispersion of the BIC that is interacting with the J-exciton in the *active* system differs from that of the bare BIC due to the presence of the J-aggregate thin film due to its refractive index (see Fig. S1d). To account for this, the photonic dispersion utilized in the coupled oscillator model corresponds to what is generally referred to the photonic dispersion of the passive system, where the bare metasurface is simulated while covered by a 25 nm thick J-aggregate film with a fixed refractive index $n=2.2$ (taken from the experimental refractive index of the J-aggregate). As shown in Fig. S4a and b, the bare and passive photonic dispersion (BIC_1) are similar in shape but differ in energy as the refractive index of the J-aggregate film causes a red-shift of the whole dispersion. While the photonic band structure of the active metasurface (Fig. S4c and d for the calculated and experimental dispersion, respectively) is considerably redshifted in energy and distorted in dispersion, hinting at strong light-matter interactions between the J-exciton and BIC_1 and the observation of the lower polariton band (BIC_1 LP).

To confirm this hypothesis, the interactions between the J-exciton and the BIC can be modelled by a coupled oscillator, which predicts the formation of the upper and lower exciton-polariton bands:

$$E_{LP,UP} = \frac{1}{2} \left[E_{exc} + E_{cav} + \frac{i(\gamma_{cav} + \gamma_{exc})}{2} \right] \pm \sqrt{g^2 + \frac{1}{4} [E_{exc} - E_{cav} + i(\gamma_{cav} - \gamma_{exc})]^2}$$

Plugging the energy and losses of the J-aggregate, and the simulated passive cavity dispersion into the coupled oscillator model leaves the coupling strength, g , as the sole fitting parameter. The coupling strength is thus determined by minimizing the error between the calculated lower

polariton dispersion and the experimental lower polariton emission. The Rabi splitting, $\hbar\Omega$, is

$$\text{calculated from the coupling strength based on the formula } \hbar\Omega = 2\sqrt{g^2 + \frac{(\gamma_{cav} - \gamma_{exc})^2}{4}}.$$

The calculated upper and lower polariton bands are showed Fig. S4d, with the lower polariton matching the experimental dispersion when the Rabi splitting is calculated to be $\hbar\Omega_{LP-1} = 305\text{meV}$, while the upper polariton is not observed due to the strong absorption of the TDBC film in the predicted spectral region. The same fitting procedure is performed for the two other metasurfaces, yielding Rabi splittings of $\hbar\Omega_{LP-2} = 320\text{ meV}$ and $\hbar\Omega_{LP-3} = 328\text{ meV}$.

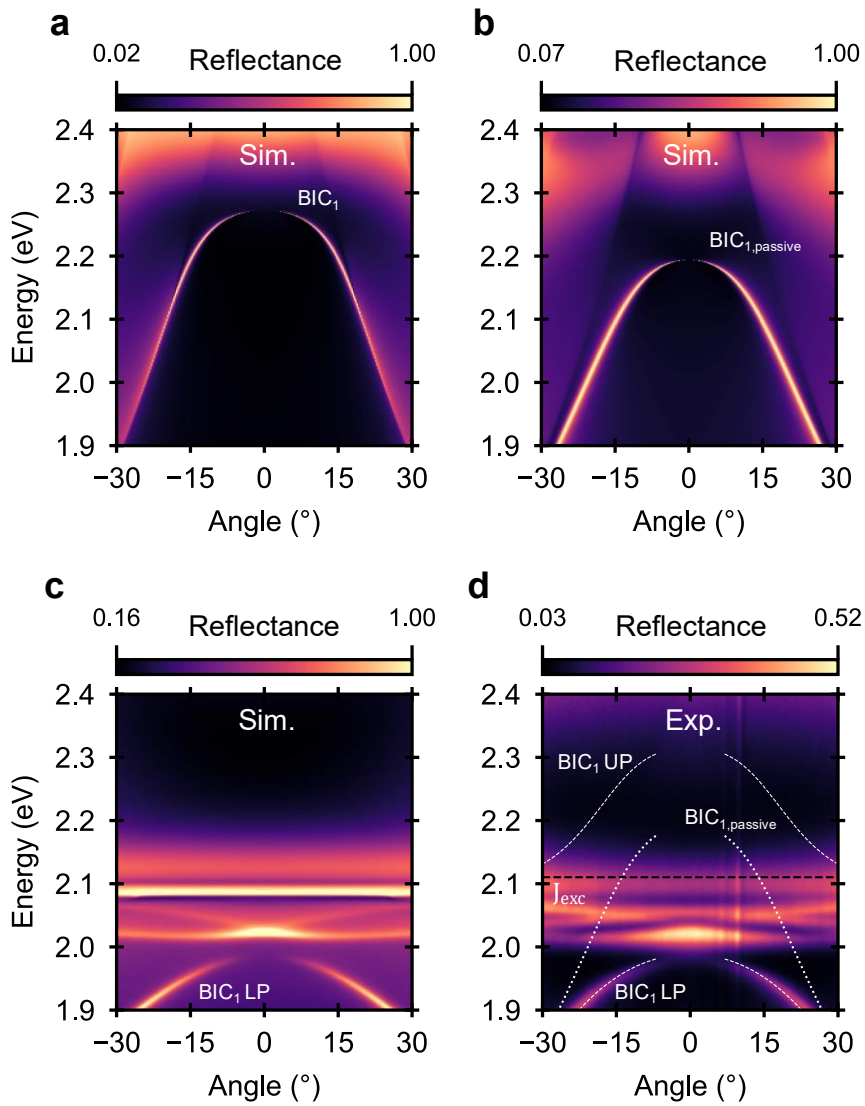


Fig. S4: Calculated photonic dispersions of the metasurface BIC resonance **a-b,**

Calculated angle-resolved reflectance of the bare (a), passive (b), and active (c) metasurface showing the typical dispersion of a BIC for the bare and passive metasurface (BIC_1 and $BIC_{1,passive}$, respectively), while the active metasurface shows significant redshift and distortion of the BIC band as expected from a lower polariton band ($BIC_1 LP$). d, Experimental angle-resolved reflectance of the active metasurface where the coupling between the J-exciton (black dashed line) and the passive BIC (white dotted line) results in the formation of the upper and lower polariton bands (white dashed lines). The upper and lower polaritons are calculated via the coupled oscillator model with a calculated Rabi splitting $\hbar\Omega_{LP-1} = 305$ meV.

Superradiance in J-aggregates

Time-resolved photoluminescence measurements are performed to confirm the superradiant nature of the J-aggregate emission. The TDBC monomer powder was dispersed in methanol to prevent aggregation, and was then cast on glass via spin coating to form a film.

Figure S5a shows a typical emission curve of the monomer film (blue dotted line) measured with a time-resolved photoluminescence setup. By fitting the emission decay with an exponential function, we extracted a monomer lifetime of 1480 ps. Similarly, the J-aggregate film time response is measured (orange solid line in Fig. S5a) and its amplitude average lifetime is extracted to be 274 ps after deconvolution with the instrument response function, revealing a significant reduction of the lifetime, in accordance with other references in literature^{34,36,70,71}.

To characterize the dependence of superradiant emission on the number of excited J-aggregates, time-resolved measurements are performed as a function of excitation density. The peak intensity of the time-resolved PL of the bare J-aggregate film and of the lower polaritons is shown to grow super-linearly with excitation density (Fig. S5b), following a power law with exponents increasing from 1.12 to 1.55 along with the Rabi splitting (dashed lines). The

superlinear scaling of the emission peak intensity with excitation density is a hallmark signature of superradiance^{3,26,72,73}, a direct consequence of the emission speed-up when an increasing number of emitters is participating in cooperative emission. While the increase in power law exponent with growing Rabi splitting confirms the enhanced non-linearity induced by the metasurface.

Furthermore, the lifetime of both the J-aggregate film and the lower polaritons decrease as a function of excitation density (Fig. S5c), with the lower polaritons systematically having a shorter lifetime than the J-aggregate uncoupled emission. In Fig. S5d, the lifetime of the bare and the strongly coupled J-aggregates are utilized to calculate the average number of coherent excitons $N = \frac{\tau(N_{coh})}{\tau_J}$, where $\tau(N_{coh})$ represents the lifetime of the J-exciton when each exciton

has a delocalization length of $N_{coh} = 5.44 \sqrt{\frac{|J|}{W}} - 1 = 7$ as determined in [49]. The emission speed-up observed in the system can thus be associated to two superradiant regimes⁵⁸: *microscopic* superradiance, originating from the formation of delocalized excitons with a macrodipole of N_{coh} molecular units, and *macroscopic* superradiance arising from coherent coupling of distinct J-excitons (reaching a maximum of 4 interacting J-excitons at the largest excitation density measured in Fig. S5d, in line with predictions found in literature³⁹).

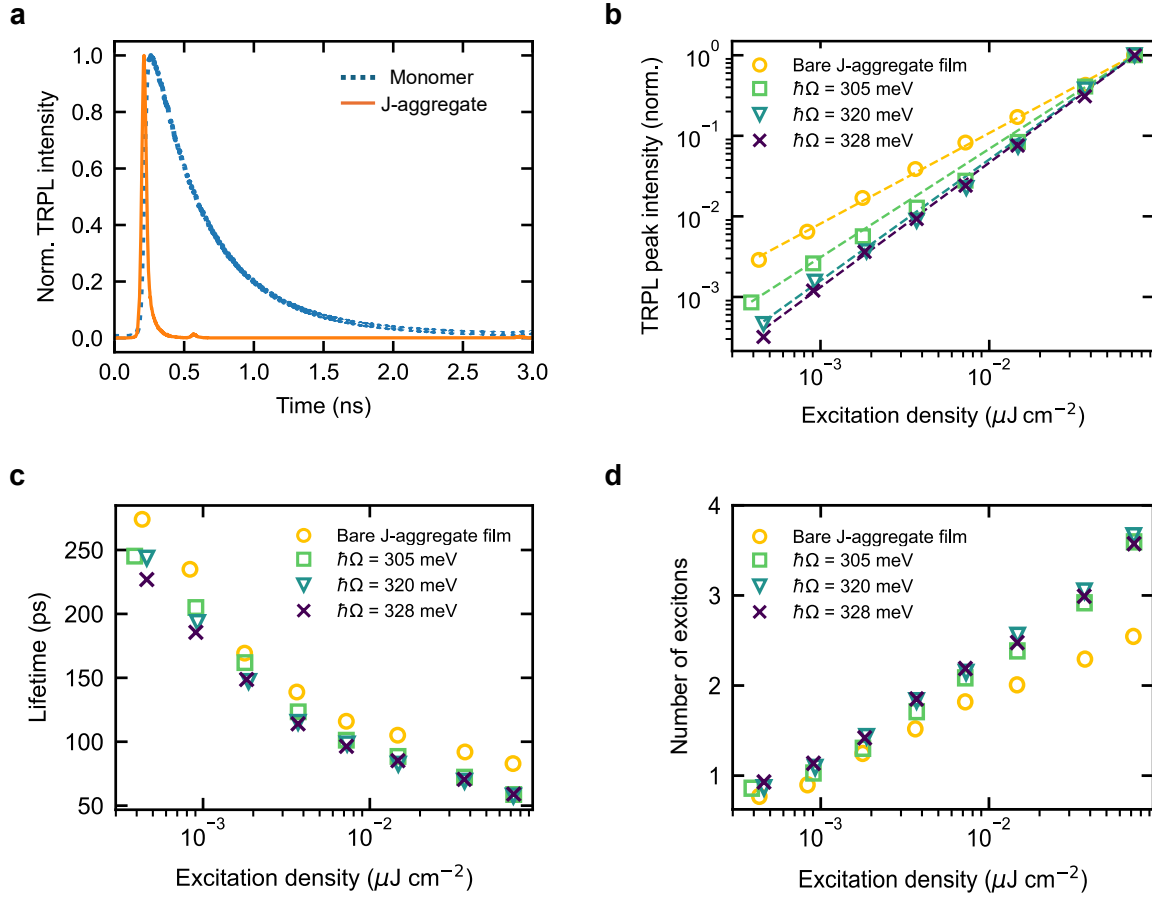


Fig. S5: Superradiance in the time-resolved regime

a, Normalised time-resolved photoluminescence curves of the monomer (blue dotted line) and J-aggregate (orange solid line) films, showing the speed-up in decay as predicted by the process of J-aggregation. **b**, Peak PL intensity in time-resolved measurements for the bare J-aggregate film and lower polaritons showing super-linear growth with excitation intensity. The dashed lines represent a power law fit that yields $n=1.12$ and $n=1.55$ for the J-exciton and BIC₃ LP, respectively. **c**, Extracted lifetime of the J-exciton state (yellow circles) and lower polaritons demonstrating the typical power-dependent decay speed-up of superradiant emitters. **d**, Calculated number of coherent excitons (N) as a function of excitation density for the uncoupled J-aggregate film and the lower polaritons, showing that the number of interacting coherent excitons increases with excitation density and Rabi splitting up to a maximum of 4.

It is also of interest to study the steady-state PL intensity dependence on excitation density for a superradiant system⁷⁴⁻⁸¹. From the definition of quantum yield, $\Phi = \frac{I_E}{I_A} = \frac{k_r}{k_r + k_{nr}}$, where I_E

and I_A represent the emitted and absorbed light intensity respectively, and k_r and k_{nr} are the radiative and non-radiative emission rates, it can be seen that any excitation density dependent scaling of the emission rates will inevitably change the quantum yield and thus the power dependent steady-state response of the system. Considering that for superradiant emitters the radiative rate grows with power due to the increase in coupled units following the relation $k_r = k_r(I) \propto N(I) k_{r,monomer} \propto I_A^{26}$, the quantum yield scaling will depend on the ratio between k_r and k_{nr} . When $k_{nr} \gg k_r$, as commonly found in J-aggregate films⁵³, we obtain $I_E = \Phi I_A = \frac{N k_{r,monomer}}{N k_{r,monomer} + k_{nr}} I_A \propto \frac{I_A}{I_A + k_{nr}} I_A \propto \frac{I_A}{k_{nr}} I_A \propto I_A^2$ which predicts a quadratic growth of the emitted intensity as observed in the experimental steady-state PL from BIC₃LP (Fig. 4h), and a linear to super-linear (up to quadratic) growth for lower Rabi splittings (Fig. 4f-g) and the uncoupled J-aggregate (Fig. 4e) due to their lower radiative rate. It should be noted that this description is valid for a system comprised of superradiant emitters in the absence of a background of uncorrelated emission with constant quantum yield. A complete description of the quantum yield dependence on power for a realistic system requires a more detailed analysis that accounts for both contributions.

Photon statistics of J-aggregates and Rhodamine-B films

An extended version of the experimental $g^{(2)}(\tau)$ discussed in the manuscript is shown in Fig. S6a-d (lowest excitation density) and f-i (maximum excitation density), where $g^{(2)}(\tau)$ peaks at short time delays ($\tau = 0$ ps) and decays to constant coincidence values at large delays (where the coincidences are used for normalization). The extended tails of $g^{(2)}(\tau)$ for large time delays are typical of nonradiative dark or longlived states that may give rise to intermittent emission or blinking^{82,83}.

Furthermore, a rhodamine-B film was used as a control sample and its $g^{(2)}(\tau)$ was measured both for the bare film (Fig. S6e) and for a resonant metasurface covered by the film (Fig. S6j). In both cases, rhodamine-B does not display any significant changes in its photon statistics.

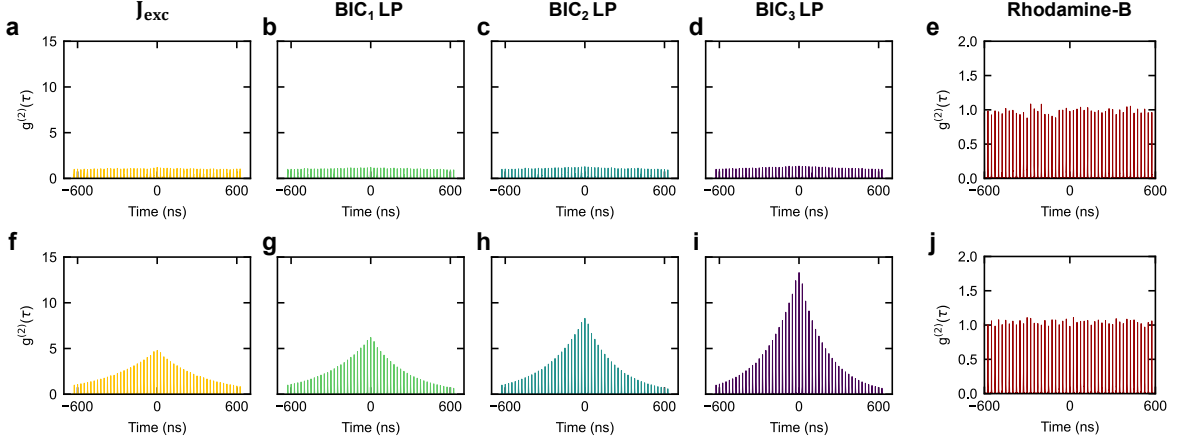


Fig. S6: Intensity correlation measurements of J-aggregates and Rhodamine-B films

Extended view of the full intensity correlation function for the **a-d**, lowest and **f-i**, highest excitation density. These curves have been used to extract the zero delay time values discussed in the main text and reported in Fig. 5. **e** and **j**, show the intensity correlation function for a bare and a metasurface-coupled Rhodamine-B film, respectively. In either case there is no significant change to the photon correlations.

Modelling the second order correlation function in superradiant J-aggregates

To model the second order correlation function, we consider a simplified model: a train of well-distinguished optical modes (“pulses”) with amplitude \hat{a}_n separated by interval τ . These modes emerge as a result of pumping a quantum light source with a pulsed laser with repetition rate τ . The distance between the modes is large compared to all the timescales of the source, so that pulses are independent and $[\hat{a}_n, \hat{a}_m^\dagger] = \delta_{nm}$. Each mode is prepared in the same quantum state described either by a wavefunction $|\psi\rangle_n = |\psi\rangle$ or a density matrix $\rho_n = \rho$.

Detectors of the HBT setup are synchronized with the pulses and their integration time is larger than the pulse width. The separability of the modes allows us to write the second-order correlation function as:

$$g^{(2)}(t) \equiv g^{(2)}(n\tau) = \begin{cases} \frac{\text{Tr}\{\rho_n \otimes \rho_0 \hat{a}_n^\dagger \hat{a}_0^\dagger \hat{a}_0 \hat{a}_n\}}{\text{Tr}\{\rho_0 \hat{a}_0^\dagger \hat{a}_0\}^2} & \text{for } n \neq 0, \\ \frac{\text{Tr}\{\rho_0 \hat{a}_0^\dagger \hat{a}_0^\dagger \hat{a}_0 \hat{a}_0\}}{\text{Tr}\{\rho_0 \hat{a}_0^\dagger \hat{a}_0\}^2} & \text{for } n = 0. \end{cases}$$

Due to the lack of correlations between the modes, the numerator in the first line factorizes as:

$$\text{Tr}\{\rho_n \otimes \rho_0 \hat{a}_n^\dagger \hat{a}_0^\dagger \hat{a}_0 \hat{a}_n\} = \text{Tr}\{\rho_n \otimes \rho_0 \hat{a}_n^\dagger \hat{a}_n \hat{a}_0^\dagger \hat{a}_0\} = \text{Tr}\{\rho_n \hat{a}_n^\dagger \hat{a}_n\} \text{Tr}\{\rho_0 \hat{a}_0^\dagger \hat{a}_0\} = \text{Tr}\{\rho_0 \hat{a}_0^\dagger \hat{a}_0\}^2,$$

and $g^{(2)}(n\tau)$ takes unity value for $n \neq 0$. Moreover, since both numerator and denominator contain normal ordering of annihilation and creation operators, only photon number distribution is of importance, while the state coherence plays no role. The formalism introduced above is now utilized to model the photon correlations of the emission originating from a number of M J-aggregates each hosting N J-excitons with probability of emission P_{emit} and interaction strength $J^{(m-m)}$ where m is the inter-aggregate coupling order (large values of m are associated to a large number of J-excitons being coherently coupled). In this system, each mode is described by the binomial distribution (probabilistic emission of zero photons, or N photons, or $2N$ photons, ..., or MN photons):

$$\rho_n = \rho_{B.D.} = \sum_{k=0}^M \binom{M}{k} P_{emit}^k (1 - P_{emit})^{M-k} |Nk\rangle \langle Nk|.$$

The corresponding average operators are

$$\text{Tr}\{\rho_{B.D.} \hat{a}_0^\dagger \hat{a}_0\} = \sum_{k=0}^M \binom{M}{k} P_{emit} (1 - P_{emit})^{M-k} Nk,$$

$$\text{Tr}\{\rho_{\text{B.D.}} \hat{a}_0^\dagger \hat{a}_0^\dagger \hat{a}_0 \hat{a}_0\} = \sum_{k=0}^M \binom{M}{k} P_{\text{emit}}^k (1 - P_{\text{emit}})^{M-k} Nk(Nk - 1).$$

Considering that increasing the cavity-exciton coupling strength promotes inter-aggregate coupling⁴⁷, when the J-aggregates are coupled to resonant metasurfaces the coupled system will be driven toward a regime of more coherently interacting aggregates, each emitting more photons, with the maximum number of emitted photons fixed at $M \times N$.

The resulting $g^{(2)}(0)$ will grow as the number of coupled emitters increases when the source is probabilistic ($P_{\text{emit}} < 0.99$), owing to the build-up of correlation between coupled aggregates. This is shown in Fig. S7, where the $g^{(2)}(0)$ -function is flat at $g^{(2)}(0) = 1$ for a deterministic source ($P_{\text{emit}} = 0.99$) regardless of the number of interacting aggregates, while it is quickly increasing for a probabilistic source, with the value of $g^{(2)}(0)$ inversely proportional to the probability of emission. The maximum value of $g^{(2)}(0)$ is obtained for a source with low probability of emission where all J-excitons are coupled to each other. A realistic scenario of the model is shown in Fig. 5d, where $N = 4$ as extracted from the experimental data in Fig. S5d and as previously observed in literature³⁹, and the probability of emission is fixed to $P_{\text{emit}} = 0.02$ ^{53,54}. Furthermore, based on the experimental excitation density and the assumed P_{emit} , we estimate the total number of photons exciting a volume of $t \times \lambda^2$ and thus the maximum number of excited J-aggregates as $M = \frac{P\lambda^3}{hc} P_{\text{emit}} \sim 2^{10}$ where P is the fluence and λ is the emission wavelength. This estimate will be used as the total number of J-aggregates to calculate the number of cooperative J-excitons (Fig. 5b) and in the $g^{(2)}(0)$ model (Fig. 5d).

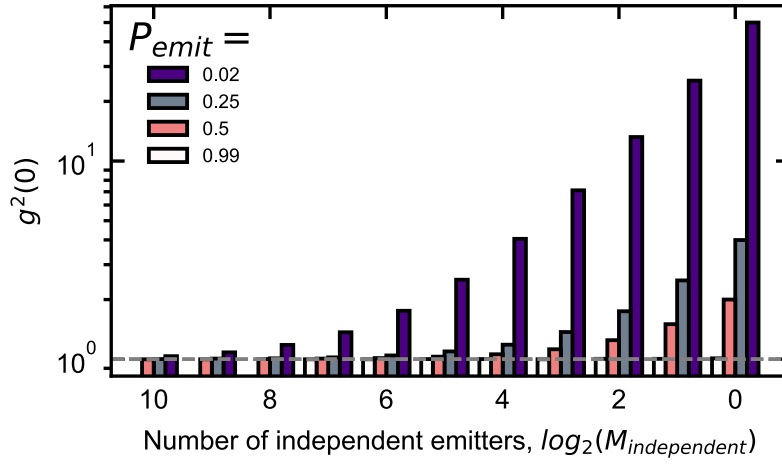


Fig. S7: Photon correlations in the inter-aggregate emission regime Calculated $g^{(2)}(0)$ for deterministic ($P_{emit} = 0.99$) and probabilistic sources ($P_{emit} < 0.99$) as a function of the number of independent emitters. The correlation function shows photon bunching for probabilistic sources with magnitude inversely proportional to the number of coupled units and flattens to 1 as the source approaches a deterministic multi-photon regime, becoming completely flat for a deterministic source.